

Observation of two-dimensional Anderson localisation of ultracold atoms

Donald H. White,^{1,2,*} Thomas A. Haase,^{1,2,†} Dylan J. Brown,^{1,2} Maarten D. Hoogerland,^{1,2} Mojdeh S. Najafabadi,^{1,3} John L. Helm,^{1,3} Christopher Gies,⁴ Daniel Schumayer,^{1,3} and David A. W. Hutchinson^{1,3}

¹*Dodd-Walls Centre for Photonic and Quantum Technologies, New Zealand*

²*Department of Physics, University of Auckland, Auckland, New Zealand*

³*Department of Physics, University of Otago, Dunedin, New Zealand*

⁴*Institut für Theoretische Physik, Universität Bremen, Bremen, Germany*

I. ABSTRACT

Anderson localisation —the inhibition of wave propagation in disordered media— is a surprising interference phenomenon which is particularly intriguing in two-dimensional (2D) systems. While an ideal, non-interacting 2D system of infinite size is always localised, the localisation length-scale may be too large to be unambiguously observed in an experiment. In this sense, 2D is a marginal dimension between one-dimension, where all states are strongly localised, and three-dimensions, where a well-defined phase transition between localisation and delocalisation exists as the energy is increased. Here we report the results of an experiment measuring the 2D transport of ultracold atoms between two reservoirs, which are connected by a channel containing pointlike disorder. The design overcomes many of the technical challenges that have hampered observation of localisation in previous works. We experimentally observe exponential localisation in a 2D ultracold atom system.

II. INTRODUCTION

Anderson localisation [1] is a phenomenon resulting from wave interference between multiple propagation paths, and has been observed in a variety of wave systems [2–18]. While it is a single-particle phenomenon, its nature is affected by numerous factors including interparticle interactions [19, 20], dimensionality [21], time-reversal symmetry [22], spin-orbit coupling [23], and the microscopic nature of the disorder [24]. A full understanding of the physics of Anderson localisation demands experimental control of these parameters. Ultracold atoms have proven to be among the cleanest and most controllable of all quantum mechanical systems [25], and have thus provided a natural avenue for modern experiments on Anderson localisation.

Careful experiments in 1D with weakly- [26] and non-interacting [27] atoms expanding in a waveguide contain-

ing optically-generated disorder allowed for unambiguous observation of Anderson localisation. These were followed by experiments demonstrating Anderson localisation in 3D [28, 29], and by studies of the metal-insulator transition [30].

In parallel to this, experiments with cold atoms in 2D have shown behaviours characteristic of weak localisation [31–33]. However, unambiguous observation of Anderson localisation in 2D real-space cold atom systems has, to our knowledge, not previously been observed. This has been due to two main challenges. First, the localisation length in 2D depends exponentially on the particle energy [3, 34]: for experimentally feasible particle energies, observing localisation requires large systems ($> 100\mu\text{m} \times 100\mu\text{m}$) even for ultracold atoms. The optically disordered potential landscapes must have high optical resolution over the entire domain, because the scatterer size must be smaller than the atomic de Broglie wavelength (equivalently, the spatial Fourier components of disorder must exceed the majority of atomic momenta). Secondly, while optical speckle patterns provide appropriate disorder for 1D and 3D systems, the statistics of optical speckle are problematic in 2D due to the high classical percolation threshold [35]. Observing Anderson localisation in 2D on reasonable length-scales, therefore, requires relatively strong scattering, and this leads to difficulty in distinguishing localisation effects from classical trapping; low energy particles have the shortest localisation lengths, yet they are also trapped classically by the optical speckle. To this end, Morong and DeMarco suggested the use of randomly positioned point scatterers [35], which allows for a tuneable percolation threshold based on the amount of disorder, and thus allows for quantum interference effects to be effectively isolated from trapping effects.

In this work we implement point scatterers in a 2D plane by projecting a blue-detuned 532 nm optical pattern shaped by a spatial light modulator (SLM) onto a flat, large-area two-dimensional trap formed from 1064 nm light [36]. The SLM enables any arbitrary potential to be projected onto this plane. We take advantage of this flexibility and project the outline of an additional dumbbell-shaped container consisting of two reservoirs separated by a channel [37, 38], with point scatterer disorder located in the channel. Atoms from a ^{87}Rb Bose–Einstein Condensate (BEC) are loaded into the source reservoir, and propagate through the channel into the drain reservoir. The transmissive nature of

* Present address: Department of Applied Physics, Waseda University, Shinjuku, Tokyo, Japan

† D. H. W. and T. A. H. contributed equally to this work.

this experiment has four main advantages compared to traditional expansion experiments with ultracold atoms [39]. Firstly, the fraction of atoms collected in the source and drain reservoirs provides a measurement of the effective resistance of the disordered channel. The measurement of the atom number in a finite reservoir provides a larger signal-to-noise ratio than is accessible with an expansion experiment. Secondly, measuring the atom distribution within the channel enables us to identify the onset of strong localisation as the channel density profile becomes exponential. The two complementary measurements, of the resistance and the channel profile, provide rich information on the transport properties of the disordered channel. Thirdly, the transmissive nature of the experiment allows us to arbitrarily change the length and width of the atom container, and thus to observe the atom transport on length scales both shorter and longer than the localisation length ξ . Finally, in a transport experiment the Bose gas is not in thermal equilibrium, which suppresses the formation of a Lifshits glass [40, 41] (the mixture of low-energy single-particle localised states could mistakenly be identified as Anderson localisation). With these advantages, we tune between the weak- and strong-localised regimes [42], and observe compelling evidence for Anderson localisation of ultracold atoms in 2D.

III. METHODS

A BEC of ^{87}Rb atoms is initially prepared in a crossed-beam CO_2 laser optical dipole trap and $\sim 1.6 \times 10^4$ atoms in the $|F = 1, m_F = -1\rangle$ state are loaded into a large-area quasi-2D trap, as illustrated in Fig. 1. The trap is created by interfering two elliptical beams (1.8 mm-to-8 mm height-to-width ratio), each of 5.0 W of 1064 nm light at an angle of 6° . The resulting light sheets are vertically spaced by $8 \mu\text{m}$, while the initial diameter of the three-dimensional BEC is $\sim 2 \mu\text{m}$. This allows the ~ 5 nK atoms to load into a single light sheet, with characteristic trap frequencies of $\nu_x = \nu_y = 1$ Hz, $\nu_z = 800$ Hz. This geometry produces a nearly flat potential in the horizontal dimensions, allowing near-ballistic transport with the exception of a weak long-period in-trap interference fringe [50].

A custom optical potential, produced with an image of a 1280×768 pixel Holoeye LC-R 720 spatial light modulator (SLM) is then projected onto the working plane. The image is generated with blue-detuned 532 nm light, and imaged with an in-vacuum aspheric lens of numerical aperture 0.42 to give a resolution of $0.9 \mu\text{m}$. A single SLM pixel has dimensions $20 \mu\text{m} \times 20 \mu\text{m}$, which with a magnification of 0.036 translates to a dimension of $0.72 \mu\text{m} \times 0.72 \mu\text{m}$ in the image plane. The setup allows any custom potential to be drawn, and we image a dumbbell-shaped boundary of two reservoirs of radius r separated in the x direction and linked by a channel of length L and width w . The channel contains customizable, point-like, optical disorder, produced by images of

randomly located blocks of 2×2 SLM pixels. In the image plane these manifest as approximately Gaussian potential hills of full-width-at-half-maximum $\sigma = 1.4 \mu\text{m}$ and 5 nK amplitude.

Atoms are loaded at the centre of the source reservoir and propagate through the channel into the drain reservoir for an expansion time t after the CO_2 laser crossed-beam trap is released. The atoms initially expand due to repulsive atom-atom interactions, acquiring kinetic energy and a mean wavenumber of $k \approx 1.6 \mu\text{m}^{-1}$. The

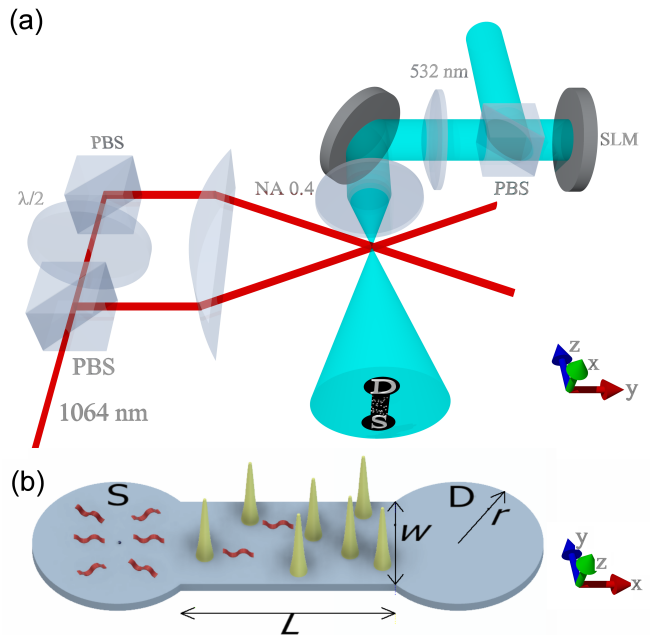


FIG. 1. **Experimental setup.** (a) The two-dimensional trap is produced by interfering two 1064 nm beams, focused with a 250 mm focal length cylindrical lens. The beams intersect at a relative angle of 6° producing horizontal pancake-like interference fringes in the vacuum chamber where the BEC is prepared in a crossed-beam CO_2 laser optical dipole trap. Atoms from the BEC are loaded into a single light sheet. Simultaneously, a wide and uniform beam of blue-detuned 532 nm light (top right) is reflected from the spatial light modulator (SLM), with a dumbbell-shaped mask applied. Disorder is located within the channel connecting the two reservoirs of the dumbbell. The polarising beamsplitter (PBS) converts the spatial polarisation modulation of the SLM to intensity modulation, which is imaged onto the atomic plane using two lenses. The in-vacuum aspheric lens of numerical aperture 0.42 provides a resolution of $0.9 \mu\text{m}$. An example of the dumbbell-shaped combined red and blue optical potentials at the atomic plane are shown in the expanded bottom right bubble. Atoms are loaded into the source (S) reservoir and propagate through the channel into the drain reservoir (D). (b) Atoms are released from the CO_2 laser trap at the centre of the source reservoir, and propagate as matter waves (red) into the disordered channel and drain reservoir. The radius r , channel length L and channel width w are illustrated. Point disorder within the channel is illustrated as a series of potential hills.

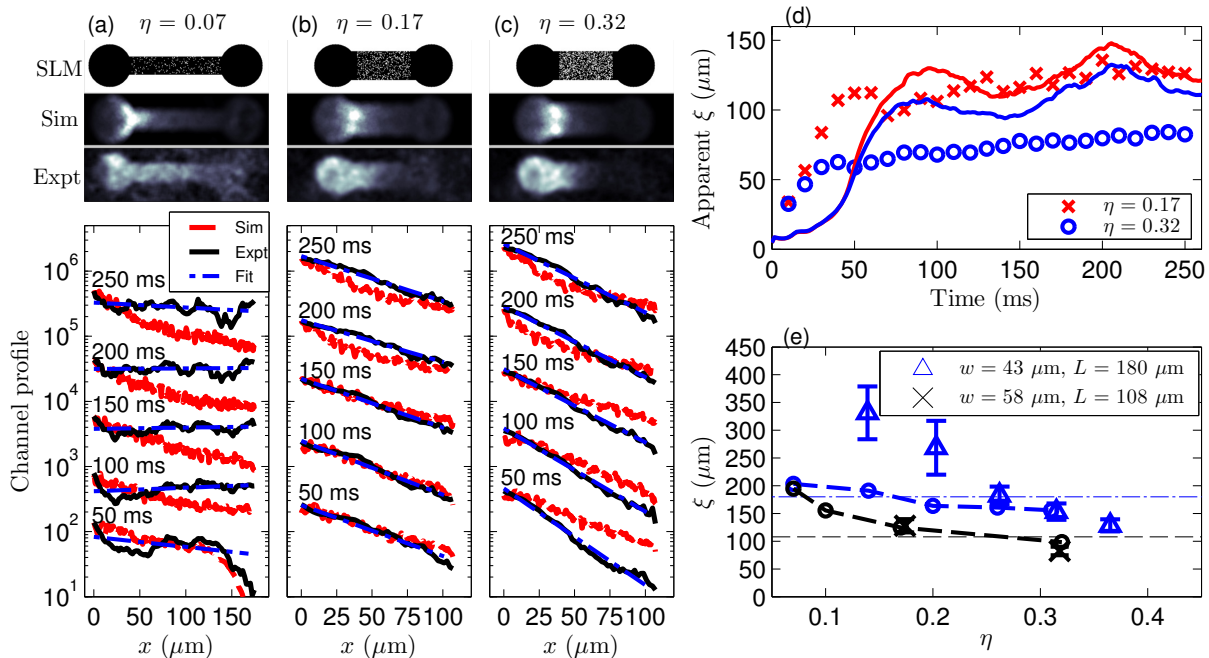


FIG. 2. **Observation of exponential channel density profiles.** (a-c) The top images in each column show the mask applied to the spatial light modulator (white indicates bright pixels). The second row of images shows the density obtained from Gross-Pitaevskii simulations after 250 ms. The third row of images show an average of three experimental absorption images after 250 ms of evolution, each with different disorder realisations. The channel density profiles show semi-logarithmic snapshots of the channel density (in units of atoms per $2.1 \mu\text{m}$ camera pixel length), at times (50, 100, 150, 200, 250) ms of time evolution, with the density integrated across the y -direction. Each increasing-time snapshot is offset for clarity by a factor of 10. Profiles are overlaid with an exponential fit to the data in blue, and with the density profiles from the GPE simulation in red. Details of the geometry are: (a) $\eta = 0.07$, $(r, L, w) = (43, 180, 36) \mu\text{m}$; (b) $\eta = 0.17$, $(r, L, w) = (43, 108, 58) \mu\text{m}$; (c) $\eta = 0.32$, $(r, L, w) = (43, 108, 58) \mu\text{m}$. (d) The apparent localisation length is found at each time evolution from the weighted exponential fit to the channel profile for two values of η , with $(r, L, w) = (43, 108, 58) \mu\text{m}$. Results from GPE simulations are shown as solid lines. (e) The localisation length is found as an average of apparent localisation lengths for times 210–250 ms, for two channel geometries. Numerical simulation data is also plotted (joined circles). Errorbars show standard deviations obtained from three trials with different disorder realisations. Dotted lines indicate the channel lengths of $180 \mu\text{m}$ and $108 \mu\text{m}$ of the two different geometries. Note that the experimental data for $w = 58 \mu\text{m}$ is shown for $\eta = 0.17$ and $\eta = 0.32$ only.

disorder correlation length is approximately one quarter of the de Broglie wavelength, giving the wave scattering properties which allow for Anderson localisation, especially for atoms with energies lower than the mean energy.

Once the atoms have been loaded into the 2D trap, they are left to expand through the channel into the second reservoir. We impart a weak slope to the trap, giving a gravitational acceleration of $\sim 0.002 \text{ m/s}^2$ along the longitudinal direction and thereby atoms acquire $\sim 0.6 k_B T$ of kinetic energy while crossing a $150 \mu\text{m}$ channel. This linear potential assists the transport by compensating for a weak fringing barrier [50] at the opening of the source reservoir and it is analogous to a weak voltage applied to an electronic thin film in order to obtain a resistance measurement. For sufficiently weak bias, Anderson localisation is expected to be maintained [51]. Data acquisition is performed by capturing a series of absorption images, with imaging resolution of $8 \mu\text{m}$, at different expansion times within the dumbbell in steps

of 10 ms up to 250 ms. Example absorption images are shown in the ‘Expt’ panels of Fig. 2(a)-(c). For each fill-factor the experiment is repeated three times, each time with a different disorder realisation to perform configurational averaging.

The disorder is characterised by its fill-factor η , defined as: $\eta = A_{\text{disorder}}/A_{\text{channel}} = n\sigma^2$, where n is the density of scatterers and $\sigma = 1.4 \mu\text{m}$ is the effective scatterer width. Equivalently, η is the fraction of bright pixels within the channel displayed by the SLM. Note that the classical percolation threshold of point scatterer disorder is negligible for $\eta \lesssim 0.06$ and remains below that of the optical speckle up to $\eta \lesssim 0.35$ [35]. In referring to Ref. [35], note that our definition of fill-factor differs by a factor of 2, i.e. $\eta = 2nw^2$.

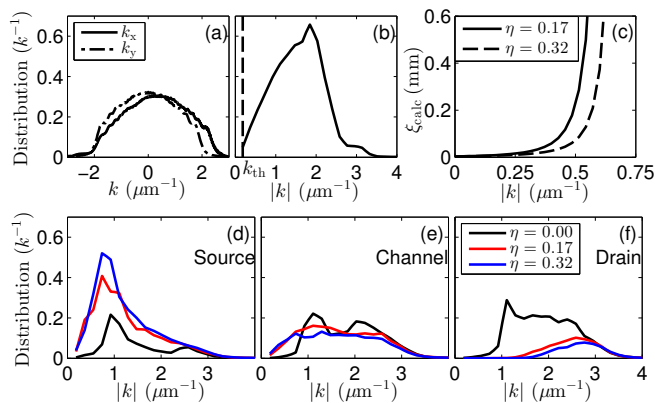


FIG. 3. **Momentum distribution of atoms and the link to localisation length.** (a) Numerical simulation showing the initial momentum distribution in the x and y directions, following the interaction-driven expansion after release from the harmonic trap, and prior to entering the channel (40 ms of expansion). (b) Distribution of initial absolute momentum value, with a mean of approximately $1.6 \mu\text{m}^{-1}$. The classical trapping threshold is indicated as the dashed line annotated by k_{th} . (c) Theoretical localisation length as a function of $|k|$, as calculated from Kuhn *et al.* for two fill-factors [34]. Following 250 ms of expansion in the numerical simulation, the k -distribution in the three dumbbell regions of a $L = 108 \mu\text{m}$ dumbbell is plotted for three fill-factors for (d) the source reservoir; (e) the channel; and (f) the drain reservoir. The scale is chosen such that the integral of each distribution reflects the sum of atoms in that region of the dumbbell.

IV. RESULTS

A. Theory

Our experimental observations are complemented with a systematic numerical analysis in order to understand the experimental findings in more detail and to support their interpretation. On a fundamental level Anderson localisation is a single-particle phenomenon, therefore, its appearance in a quantum system can be captured by a one-body Schrödinger equation with a potential term, $V_{\text{trap}}(\mathbf{r})$, corresponding to the confinement and to the 2D static disorder. However, in the experiment some weak interaction, $V_{\text{int}}(\mathbf{r})$, is still present between the particles. The interplay between interactions and localisation is a topic of rigorous debate [19]. We note several theoretical studies suggest that localisation is maintained in the presence of weak interactions in 1D [43–45], as well as experiments in the many-body localised regime of strong interactions [46, 47]. In the presence of interactions the dynamics are governed by the Gross–Pitaevskii equation [48] (GPE)

$$i\hbar \frac{\partial \psi}{\partial t} = \left[-\frac{\hbar^2}{2m} \nabla_{2\text{D}}^2 + V_{\text{trap}}(\mathbf{r}) + V_{\text{int}}(\mathbf{r}) \right] \psi, \quad (1)$$

which we solve using the adaptive, fourth-order Runge-Kutta-Fehlberg method [49]. Our numerical simulations

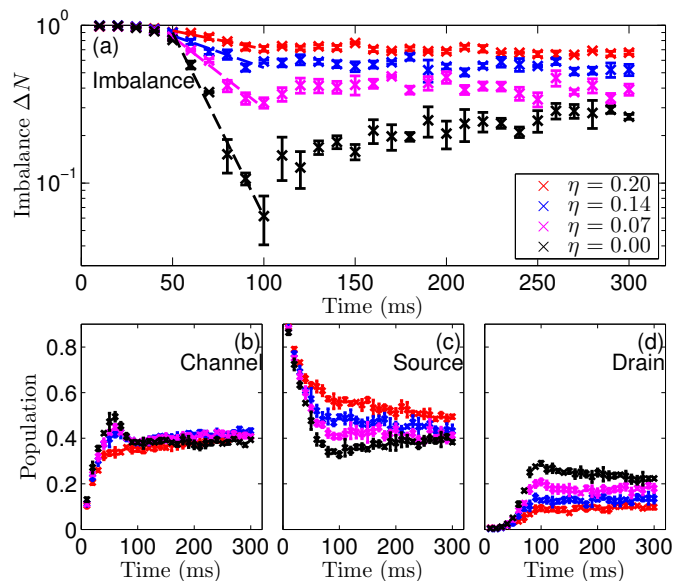


FIG. 4. **Temporal evolution of atom populations.** (a) The number imbalance ΔN vs time for four different fill-factors, with $(r, L, w) = (43, 162, 36) \mu\text{m}$. Plots are overlaid with the linear fits to the semilogarithmic plot used to calculate the resistance via Eq. (4). (b) Evolution of the channel population. (c) Evolution of the source reservoir population. (d) Evolution of the drain reservoir population. The error bars show standard deviations in the data, over 3 disorder realisations.

give access to all experimentally observed quantities and we present them alongside of the experimental measurements for comparison. A further advantage of the numerical simulations is that they allow us to switch off the interactions following the initial expansion, allowing us to analyse the effect of interactions on Anderson localisation [50].

B. Evolution of Channel Density Profiles

The experimental setup consists of ultracold atoms propagating from a source reservoir, through a disordered channel, and into a drain reservoir. The optical setup is illustrated in Fig. 1(a), the dumbbell-shaped architecture of the environment is illustrated in Fig. 1(b), and the setup is described in detail in Haase *et al.* [36]. We quantify the transport properties of this system in two ways. First, we analyse the long-time behaviour of the atomic density profile within the channel, which allows direct observation of exponential localisation. Second, we measure the temporal behaviour of the source, channel and drain populations (N_s, N_c, N_d). This facilitates the measurement of the transmission coefficient of the channel, which we interpret as a channel ‘resistance’ [37].

We first analyse the long-time behaviour of the system. The signature of Anderson localisation is an exponentially decaying wavefunction, such that the density

decays in space with a localisation length of ξ , as:

$$\rho(x) = \rho_0 e^{-2x/\xi}. \quad (2)$$

After many scattering events, the density of atoms within the disordered channel evolves to exhibit an exponentially decaying profile in an Anderson-localised system. Note that 2D is a special case: although there is a distribution of atomic momenta, and therefore a distribution of localisation lengths, the density profile is expected to be exponential [52]. This is a consequence of the finite (yet possibly large) localisation length for all momenta in 2D.

Figures 2(a)-(c) plot the time evolution of the channel density profile for three different fill-factors. For weak disorder, we observe a near constant density profile at short evolution times, which evolves to a non-exponential profile for long times. Highly disordered channels ($\eta \geq 0.17$) show distinctly different behaviour. All evolution times over 50 ms indicate an exponential profile. The apparent localisation length, found from the gradient of $\log(\rho(x))$ curve and plotted in Fig. 2(d), approaches a quasi-stationary value for long expansion times. The solution of the Gross-Pitaevskii equation shows similar behaviour, superimposed with an oscillation about a constant value. We extract the localisation length measurement from the mean value for expansion times larger than 200 ms and present the result in Fig. 2(e). This data indicates that we achieve a localisation length shorter than the channel length of $180 \mu\text{m}$ for $\eta \gtrsim 0.25$, with a similar threshold observed for the shorter and wider channel meeting the criterion for strong Anderson localisation. We find a clear relationship showing a reduced localisation length with increasing fill-factor. Numerical simulations give localisation lengths in reasonable quantitative agreement with experiment. We also remark on the slightly stronger localisation observed in the wider $58 \mu\text{m}$ channel compared to the $43 \mu\text{m}$ channel: while a fuller investigation of the width-dependence of the localisation length is planned for further study, here we hypothesise that the longer localisation length in the narrower channel is due to finite size effects, associated with the localisation length being significantly longer than the channel width.

We find a difference in equilibration time between theory and experiment in Fig. 2(a), though for longer times ($t > 400$ ms) we confirm that the numerical simulations do tend to a near-flat constant density profile [50]. We attribute differences between the experiment and simulation to effects which are not directly included in the simulation (including finite temperature effects, the smooth disordered potential, and the deviations from flatness in the 2D trap). While these differences may result in minor deviation between experiment and theory, both point towards Anderson localization. We also confirm that the simulations in Figs. 2(b) and 2(c) exhibit an exponential channel profile with a quasi-stationary mean localisation length for very long times in the case of $\eta \geq 0.17$, for $t > 400$ ms [50].

C. Momentum Dependence

Can we attribute the observed exponential density profiles to quantum interference (Anderson localisation)? The alternative interpretation would be classical trapping within the disordered potential for atoms with energies below the percolation threshold. The numerical simulations in Fig. 3(a) and (b) show the initial k -distribution following the interaction driven expansion from the BEC. The plot in Fig. 3(e) shows the steady state k -distribution within the channel for three different fill-factors. Based on this momentum distribution for $\eta = 0.32$, only 0.8% of atoms within the channel have an energy below the disorder percolation threshold, as calculated according to Morong and DeMarco [35]. This low fraction of classically trapped atoms allows us to be confident that any observed localisation is indeed due to quantum interference.

The momentum distributions, obtained by numerical simulation and illustrated in Fig. 3, provide further insight into the system dynamics. High energy atoms propagate into the drain reservoir. The difference in the drain momentum distributions between zero-disorder and disordered systems (Fig. 3(f)) shows that the disordered channel acts as an effective energy-filter, preventing low energy atoms ($|k| \lesssim 1.5 \mu\text{m}^{-1}$) from propagating into the drain. We interpret the complete inhibition of propagation of low-energy atoms as signifying Anderson localisation. The filtering effect is slightly stronger for $\eta = 0.32$ compared to $\eta = 0.17$. Weakly localised atoms are in an extended state of the system and are able to accumulate in the drain. The momentum distribution in the source (Fig. 3(d)) is skewed to low energy, because the dwell time within the source reservoir is inversely proportional to $|k|$. The channel (Fig. 3(e)) contains a mixture of weakly localised high-energy atoms in an extended state across the dumbbell, and strongly localised low-energy atoms. We note that the channel clearly contains a larger number of very low energy atoms ($|k| < 1 \mu\text{m}^{-1}$) when disorder is present, indicating that these low-energy atoms are localised within the channel.

In Fig. 3(c), we plot the localisation length expected according to:

$$\xi(|k|) = \ell_s e^{\pi|k|\ell_{\text{tr}}/2}, \quad (3)$$

where $\ell_s \approx \sigma/\sqrt{\eta}$ is the scattering mean free path and $\ell_{\text{tr}} = \Lambda(|k|\sigma)\ell_s$ is the transport mean free path [3, 34, 50]. The curve in Fig. 3(c), based on estimates of the mean free path within the system, predicts localisation lengths which are shorter than the system size for $|k| \lesssim 0.55 \mu\text{m}^{-1}$. We emphasise that this estimate should be considered in the context of the sensitive exponential dependence of the parameters, the specific microscopic details of the disorder, and the finite size of the system, which are not included in the general estimate of Eq. (3). We note that previous theoretical investigations

using point disorder obtained a sub-exponential dependence of $\xi(|k|)$ [35], with localisation lengths on the order of $100 \mu\text{m}$ expected up to $|k| = 6 \mu\text{m}^{-1}$, in a system with mean free paths of $\ell_s \approx \ell_{tr} \approx 2 \mu\text{m}$, similar to our experiment. We conclude that our experimental regime is within the bounds set by the established theory, in which Anderson localisation can be expected to be observed. At the same time, classical trapping plays a negligible role in the dynamics within the channel.

D. Effect of Interactions

The role which interactions play in Anderson localisation has been richly debated in the literature [3, 19, 20, 45, 46, 53]. This experiment is conducted with 1.6×10^4 atoms, resulting in an average density of ~ 1 atom / μm^2 . With this level of atomic density, the interaction energy is significantly lower than either the mean kinetic energy or the disordered potential depth. The experiment is conducted in a regime of weak repulsive interaction, and our numerical simulations indicate that the observed localisation length would be unchanged within error for the non-interacting case. Based on our numerical analysis, we estimate that interaction strengths more than 5 times the experimental interaction would be required to significantly alter the observed density profiles [50].

E. Atomtronic Analysis

For a second complementary analysis, we treat the system as an ‘atomtronic’ circuit [37] and describe the transport in terms of the atomic current flowing between two reservoirs of capacitance C but impeded by a channel resistance R . The atomic current is defined by the number imbalance between the source and drain reservoirs: $\Delta N = (N_s - N_d)/(N_d + N_s)$. Esslinger and co-workers suggested [54] the phenomenological relation

$$\frac{d\Delta N}{dt} = -\frac{\Delta N}{RC}. \quad (4)$$

The data in Fig. 4a shows the evolution of ΔN for varying fill-factors and for three timescales. In the ballistic period atoms transport across the channel and arrive at the second reservoir. In this first period, the imbalance remains unity due to an empty second reservoir. Following the ballistic time, there is a period of ~ 40 ms during which the imbalance reduces at its greatest rate. This initial transfer rate is greatest for zero disorder. In this period, we find an approximately linear relation between $\log(\Delta N)$ and time, supporting the RC circuit model (4), and we use this transport period to measure the channel resistance. Finally, the system moves into a third regime of transport, in which the number imbalance approaches a steady-state, non-zero value for finite η . This steady-state behaviour is supported by our numerical GPE simulations. We interpret this non-zero steady state number

imbalance to be a consequence of a combination of Anderson localisation, and enhanced reflection into the source reservoir due to weak localisation. We note that disorder with low fill-factor (e.g., $\eta = 0.07$) significantly reduces transport, as evidenced by the non-zero steady-state imbalance, although exponential localisation is not observed in this case (cf. Fig. 2a). The reduction in transport is a significant observation, due to the near-zero percolation threshold of $\eta = 0.07$ disorder [35].

In Fig. 4(b)-(d) we show the populations of the channel, source and drain reservoirs as a function of time. While the reservoir populations show a dependence on η , the channel population is largely independent of η and approaches a steady state. Weak localisation effects within the channel lead to an enhanced reflection coefficient into the source reservoir, and we estimate the mean dwell time within the channel to be 110 ms [55]. This estimated dwell time is largely independent of the details of the disorder and coincides with the population equilibration time. We also note that the steady-state channel population agrees with the relative area of the channel with respect to the whole dumbbell.

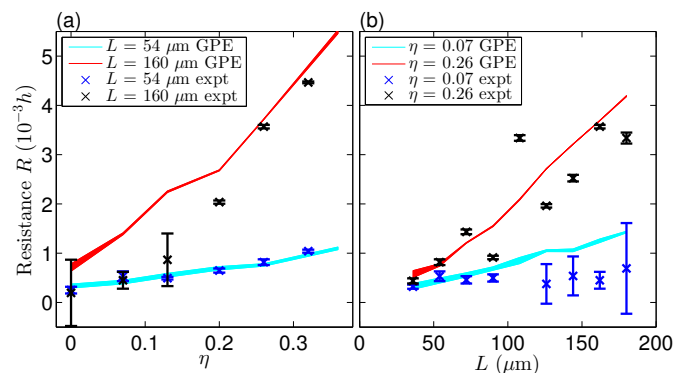


FIG. 5. **Channel resistance measurement.** (a) The resistance as a function of fill-factor, for two channel lengths, in units of Planck’s constant, with $(r, w) = (43, 36) \mu\text{m}$. (b) The resistance a function of length, for two fill-factors, with $(r, w) = (43, 36) \mu\text{m}$. Results are overlaid with GPE simulations, with the shaded region indicating one standard deviation on the simulation value. The errorbars show standard deviations in the data, over 3 disorder realisations.

The resistance in units of Planck’s constant, h , is plotted in Fig. 5 for a range of fill-factors and lengths. In this system, $\hbar C = 19$ s [50]. We observe a stronger dependence of the resistance on fill-factor for longer channel lengths; likewise, we observe a stronger dependence of the resistance on channel length for stronger disorder. While we expect the resistance to be exponential in the channel length in the strongly localised regime [21], here we observe a slower dependence within the accessible experimental parameters. Figure 3(f) shows that the atoms in the drain have significantly higher energy than the atoms in the channel or source, and we conclude that the main contribution to the resistance mea-

surement comes from atoms with very large localisation lengths and energies larger than the mean energy. We note close agreement between the experimental data and numerical simulations for the resistance measurements.

V. DISCUSSION

In conclusion, in combining a highly tuneable experimental platform with full numerical GPE simulations, we have provided compelling evidence for Anderson localisation in a two-dimensional ultracold atom system. For atoms traversing a disordered 2D potential of point scatterers in a regime of weak atomic interaction, we demonstrate clear signatures of exponential localisation. We observe temporally-stable exponential channel profiles for $\eta \geq 0.17$. The logarithm of these profiles are linear and do not change significantly for $t > 100$ ms. We have shown for our system that this localisation cannot be explained by classical trapping within the channel. The supporting numerical simulations show that transport of low energy atoms is almost totally inhibited by the disordered channel. We therefore interpret profiles with localisation lengths shorter than the channel length to signify Anderson localisation in 2D.

Through measurements of the localisation length, we

have demonstrated that the transport may be tuned via the disorder fill-factor from a regime of ballistic, to diffusive, and then to strongly localised transport with $\xi < L$. The dumbbell-shaped architecture enabled two complementary analyses, allowing measurements of the channel resistance, together with the in-channel density evolution. The channel resistance indicates that while atoms traversing weak disorder ($\eta = 0.07$) do not exhibit Anderson localisation, the transport is significantly reduced from the zero-disorder case, despite the near-zero percolation threshold. All experimental observations are supported by zero-temperature Gross-Pitaevskii calculations, and the experimental conditions are within the bounds for observation of localisation set by the established theory. The numerical simulations reproduce all signatures observed in the experiment, differing only in equilibration time. The simulations provide additional insight into the role of interactions and the momentum distributions at different fill factors, corroborating the experimental evidence, and providing strong support that Anderson localisation is the suitable interpretation of the exponential density profiles and of the reduced transport. These results provide a springboard for studying localisation and the causes of delocalisation in 2D systems with a quantum-simulator-like device.

-
- [1] P. W. Anderson, *Phys. Rev.* **109**, 1492 (1958).
 - [2] M. Cutler and N. F. Mott, *Phys. Rev.* **181**, 1336 (1969).
 - [3] P. A. Lee and T. V. Ramakrishnan, *Rev. Mod. Phys.* **57**, 287 (1985).
 - [4] R. L. Weaver, *Wave Motion* **12**, 129 (1990).
 - [5] R. Dalichaouch, J. P. Armstrong, S. Schultz, P. M. Platzman, and S. L. McCall, *Nature* **354**, 53 (1991).
 - [6] D. S. Wiersma, P. Bartolini, A. Lagendijk, and R. Righini, *Nature* **390**, 671 (1997).
 - [7] M. Stoytchev and A. Z. Genack, *Phys. Rev. B* **55**, R8617 (1997).
 - [8] C. Dembowski, H.-D. Gräf, R. Hofferbert, H. Rehfeld, A. Richter, and T. Weiland, *Phys. Rev. E* **60**, 3942 (1999).
 - [9] M. Störzer, P. Gross, C. M. Aegerter, and G. Maret, *Phys. Rev. Lett.* **96**, 063904 (2006).
 - [10] J. Topolancik, B. Ilic, and F. Vollmer, *Phys. Rev. Lett.* **99**, 253901 (2007).
 - [11] T. Schwartz, G. Bartal, S. Fishman, and M. Segev, *Nature* **446**, 52 (2007).
 - [12] H. Hu, A. Strybulevych, J. H. Page, S. E. Skipetrov, and B. A. van Tiggelen, *Nature Physics* **4**, 945 (2008).
 - [13] J. Chabé, G. Lemarié, B. Grémaud, D. Delande, P. Szriftgiser, and J. C. Garreau, *Phys. Rev. Lett.* **101**, 255702 (2008).
 - [14] F. Riboli, P. Barthelemy, S. Vignolini, F. Intonti, A. D. Rossi, S. Combrie, and D. S. Wiersma, *Opt. Lett.* **36**, 127 (2011).
 - [15] T. Sperling, W. Bührer, C. M. Aegerter, and G. Maret, *Nature Photonics* **7**, 48 (2012).
 - [16] M. Lopez, J.-F. Clément, P. Szriftgiser, J. C. Garreau, and D. Delande, *Phys. Rev. Lett.* **108**, 095701 (2012).
 - [17] I. Manai, J.-F. Clément, R. Chicireanu, C. Hainaut, J. C. Garreau, P. Szriftgiser, and D. Delande, *Phys. Rev. Lett.* **115**, 240603 (2015).
 - [18] T. Ying, Y. Gu, X. Chen, X. Wang, S. Jin, L. Zhao, W. Zhang, and X. Chen, *Science Advances* **2**, e1501283 (2016).
 - [19] S. Fishman, Y. Krivolapov, and A. Soffer, *Nonlinearity* **25**, R53 (2012).
 - [20] D. L. Shepelyansky, *Phys. Rev. Lett.* **70**, 1787 (1993).
 - [21] E. Abrahams, P. W. Anderson, D. C. Licciardello, and T. V. Ramakrishnan, *Phys. Rev. Lett.* **42**, 673 (1979).
 - [22] G. Bergmann, *Physics Reports* **107**, 1 (1984).
 - [23] G. Bergman, *Phys. Rev. Lett.* **48**, 1046 (1982).
 - [24] M. Piraud, A. Aspect, and L. Sanchez-Palencia, *Phys. Rev. A* **85**, 063611 (2012).
 - [25] I. M. Georgescu, S. Ashhab, and F. Nori, *Rev. Mod. Phys.* **86**, 153 (2014).
 - [26] J. Billy, V. Josse, Z. Zuo, A. Bernard, B. Hambrecht, P. Lugan, D. Clément, L. Sanchez-Palencia, P. Bouyer, and A. Aspect, *Nature* **453**, 891 (2008).
 - [27] G. Roati, C. D’Errico, L. Fallani, M. Fattori, C. Fort, M. Zaccanti, G. Modugno, M. Modugno, and M. Inguscio, *Nature* **453**, 895 (2008).
 - [28] S. S. Kondov, W. R. McGehee, J. J. Zirbel, and B. DeMarco, *Science* **334**, 66 (2011).
 - [29] F. Jendrzejewski, A. Bernard, K. Müller, P. Cheinet, V. Josse, M. Piraud, L. Pezzé, L. Sanchez-Palencia, and P. Aspect, *Nature Physics* **8**, 398 (2011).
 - [30] G. Semeghini, M. Landini, P. Castilho, S. Roy, G. Spagnolli, A. Trenkwalder, M. Fattori, M. Inguscio, and

- G. Modugno, *Nature Physics* **11**, 554 (2015).
- [31] M. Robert-de Saint-Vincent, J.-P. Brantut, B. Allard, T. Plisson, L. Pezzé, L. Sanchez-Palencia, A. Aspect, T. Bourdel, and P. Bouyer, *Phys. Rev. Lett.* **104**, 220602 (2010).
- [32] F. Jendrzejewski, K. Müller, J. Richard, A. Date, T. Plisson, P. Bouyer, A. Aspect, and V. Josse, *Phys. Rev. Lett.* **109**, 195302 (2012).
- [33] K. Müller, J. Richard, V. V. Volchkov, V. Denechoud, P. Bouyer, A. Aspect, and V. Josse, *Phys. Rev. Lett.* **114**, 205301 (2015).
- [34] R. C. Kuhn, C. Miniatura, D. Delande, O. Sigwarth, and C. A. Müller, *Phys. Rev. Lett.* **95**, 250403 (2005).
- [35] W. Morong and B. DeMarco, *Phys. Rev. A* **92**, 023625 (2015).
- [36] T. A. Haase, D. H. White, D. J. Brown, I. Herrera, and M. D. Hoogerland, *Review of Scientific Instruments* **88**, 113102 (2017).
- [37] S. Eckel, J. G. Lee, F. Jendrzejewski, C. J. Lobb, G. K. Campbell, and W. T. Hill, *Phys. Rev. A* **93**, 063619 (2016).
- [38] A. Li, S. Eckel, B. Eller, K. E. Warren, C. W. Clark, and M. Edwards, *Phys. Rev. A* **94**, 023626 (2016).
- [39] L. Sanchez-Palencia, D. Clément, P. Lugan, P. Bouyer, and A. Aspect, *New Journal of Physics* **10**, 045019 (2008).
- [40] I. Lifshits, S. Gredeskul, and L. Pastur, *Introduction to the theory of disordered systems*, A Wiley Interscience publication (Wiley, 1988).
- [41] P. Lugan, D. Clément, P. Bouyer, A. Aspect, M. Lewenstein, and L. Sanchez-Palencia, *Phys. Rev. Lett.* **98**, 170403 (2007).
- [42] S.-Y. Hsu and J. M. Valles, Jr., *Phys. Rev. Lett.* **74**, 2331 (1995).
- [43] P. Lugan, D. Clément, P. Bouyer, A. Aspect, and L. Sanchez-Palencia, *Phys. Rev. Lett.* **99**, 180402 (2007).
- [44] S. Lellouch and L. Sanchez-Palencia, *Phys. Rev. A* **90**, 061602 (2014).
- [45] J. Dujardin, T. Engl, and P. Schlagheck, *Phys. Rev. A* **93**, 013612 (2016).
- [46] M. Schreiber, S. S. Hodgman, P. Bordia, H. P. Lüschen, M. H. Fischer, R. Vosk, E. Altman, U. Schneider, and I. Bloch, *Science* **349**, 842 (2015).
- [47] A. Lukin, M. Rispoli, R. Schittko, M. E. Tai, A. M. Kaufman, S. Choi, V. Khemani, J. Léonard, and M. Greiner, *Science* **364**, 256 (2019).
- [48] C. Pethick and H. Smith, *Bose-Einstein Condensation in Dilute Gases* (Cambridge University Press, 2002).
- [49] R. Burden and J. Faires, *Numerical Analysis* (Brooks/Cole, Cengage Learning, 2011).
- [50] Please refer to the supplementary material for further information.
- [51] C. Crosnier de Bellaistre, A. Aspect, A. Georges, and L. Sanchez-Palencia, *Phys. Rev. B* **95**, 140201 (2017).
- [52] C. Miniatura, R. C. Kuhn, D. Delande, and C. A. Müller, *Eur. Phys. J. B* **68**, 353 (2009).
- [53] S. Donsa, H. Hofstätter, O. Koch, J. Burgdörfer, and I. Březinová, *Phys. Rev. A* **96**, 043630 (2017).
- [54] J.-P. Brantut, J. Meineke, D. Stadler, S. Krinner, and T. Esslinger, *Science* **337**, 1069 (2012).
- [55] R. Pierrat, P. Ambichl, S. Gigan, A. Haber, R. Carmignati, and S. Rotter, *Proc. Natl. Acad. Sci. U.S.A* **111**, 17765 (2014).

Acknowledgements

The authors would like to thank A. V. H. McPhail and I. Herrera for laboratory assistance, and S. S. Shamailov for detailed discussions. D. H. W. thanks L. Sanchez-Palencia and D. Delande for discussions. C. G would like to thank the German Academic Exchange Service (DAAD) for financial support during his stay at the University of Otago. This work was supported by the Marsden Fund, grant number UOA1330, administered by the Royal Society of New Zealand.

Author Contributions

M. D. H. and D. H. W. planned the research. T. A. H., D. H. W., and D. J. B. constructed the experiment. T. A. H. performed the measurements, with D. J. B. and D. H. W. providing assistance. D. J. B. and D. H. W. carried out the data analysis. J. H. wrote the Gross-Pitaevskii code. M. S. N. and D. S ran and analysed the simulations, and together with C. G and D. A. W. H. formed the theoretical underpinning. M. D. H. and D. A. W. H. supervised the experimental and theoretical work, respectively. All authors discussed the research and contributed to the manuscript.

Competing Interests

The authors declare no competing interests.

Data availability.

All data presented in this publication is available upon request.

Correspondence

Correspondence and requests for materials related to the experiment can be addressed to Maarten D. Hoogerland (m.hoogerland@otago.ac.nz), while queries regarding the theoretical investigation may be directed to David A. W. Hutchinson (david.hutchinson@otago.ac.nz).

Supplementary Material — Observation of two-dimensional Anderson localisation of ultracold atoms

Donald H. White,^{1,2,*} Thomas A. Haase,^{1,2,†} Dylan J. Brown,^{1,2} Maarten D. Hoogerland,^{1,2} Mojdeh S. Najafabadi,^{1,3} John L. Helm,^{1,3} Christopher Gies,⁴ Daniel Schumayer,^{1,3} and David A. W. Hutchinson^{1,3}

¹*Dodd-Walls Centre for Photonic and Quantum Technologies, New Zealand*

²*Department of Physics, University of Auckland, Auckland, New Zealand*

³*Department of Physics, University of Otago, Dunedin, New Zealand*

⁴*Institut für Theoretische Physik, Universität Bremen, Bremen, Germany*

Here we provide additional supporting information for the results described in the main text “Observation of two-dimensional Anderson localisation of ultracold atoms”.

I. EXPERIMENTAL DETAILS

This experiment has been designed to be a ‘quantum simulator’ of 2D transport physics. This requires full knowledge of the topography of the 2D potential landscape. Ideally, the basic 2D trap would be flat, with disorder and boundaries introduced by the SLM-projected landscape. While we approximate this condition, we have found the presence of ‘fringes’ within the 2D trap. These fringes run along the y -direction, and have a period of $\approx 150 \mu\text{m}$. The fringe depth is on the order of 5 nK. We attribute the fringes to the interference within the 1064 nm beams, which occurs from distortion to the phase-front of the beam from the vacuum window. The fringe central position may be adjusted by relative horizontal alignment of the two interfering 1064 nm beams, and we set the fringe centre to overlap the centre of the source reservoir.

The BEC is initially formed in a CO_2 crossed beam laser trap, and adiabatically loaded into the two-dimensional trap by ramping down the CO_2 laser power. Prior to the release of the CO_2 laser trap, the trap frequency in the horizontal directions is on the order of $\omega_{x,y} \approx 2\pi \cdot 50 \text{ Hz}$. The dimensionless interaction strength $\tilde{g} = a_s \sqrt{8\pi m \omega_z / \hbar} = 0.07$. The peak density within the CO_2 laser trap is $n_0 \approx \frac{m}{\hbar} \sqrt{\frac{N}{\pi \tilde{g}}} \omega_{x,y} \approx 120 \text{ atoms}/\mu\text{m}^2$. The healing length $\xi = 1/\sqrt{n_0 \tilde{g}} = 350 \text{ nm}$. The chemical potential within the CO_2 laser trap is $\mu = \hbar^2 n_0 \tilde{g} / m$, and $\mu/k_B = 40 \text{ nK}$. Once the atoms have been released from the CO_2 laser trap and expanded into the dumbbell, the density reduces to the order of 1 atom/ μm^2 , reducing the chemical potential to $\mu/k_B = 0.3 \text{ nK}$ [1, 2].

A linear slope, with acceleration 0.002 m/s, is applied to the 2D trap, meaning that atoms are no longer bound

by the fringe, and may enter the trap. While the presence of the fringe affects the bulk motion of the atoms within the channel, the period of the fringe is larger than the channel lengths used, and this means that the Anderson localisation physics should be unchanged. We note close agreement with GPE simulations (discussed below), even if the fringe pattern is excluded.

The BEC is placed such that its centre lies about half way between the centre of the source reservoir and the channel opening. We calibrate the acceleration by adjusting the tilt such that the first wave of atoms arrives at the far end of the drain reservoir at 100 ms after releasing the atoms from the dipole trap, using a 144 μm long channel.

II. FULL DATASETS

We include in Figs. 1–6 the full datasets for a range of channel widths. The data indicates that steady-state exponentially-localised channel profiles are obtained for a broad range of channel widths in the presence of disorder. The exception to this is the 14 μm width channel, where the profile is non-exponential, and exhibits a non-uniform channel profile in the case of zero applied disorder. In this case, we are in a nearly one-dimensional regime, and minor channel disorder due to imperfections in the flat disordered potential results in localised eigenfunctions. In addition, there is significant reflection at the mouth of the channel due to the small channel opening, resulting in the dropoff in channel density seen at the channel opening.

III. WIDTH DEPENDENCE

Figure 7 shows the localisation lengths extracted from the density profiles in Figs. 4–6. For $w \lesssim 50 \mu\text{m}$, the localisation length is significantly larger than the channel width and finite size effects are strong. For the quasi-2D environment of $w \gtrsim 50 \mu\text{m}$, in which the localisation length is of the same order as the channel width, we show in Fig. 7 that the width does not have a significant influence on the observed localisation length.

* Present address: Department of Applied Physics, Waseda University, Shinjuku, Tokyo, Japan

† D. H. W. and T. A. H. contributed equally to this work.

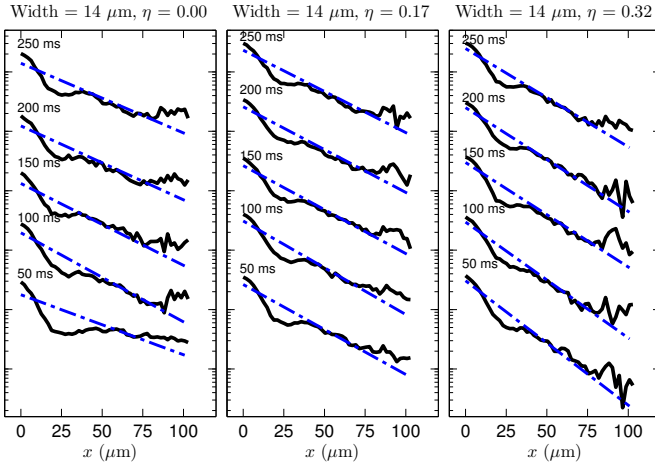


FIG. 1. $14 \mu\text{m}$ width channel density profile data. Channel profiles from 50 ms to 250 ms are plotted on a semilogarithmic scale, together with a linear fit to the logarithmic data. This data is an average of three experimental disorder realisations.

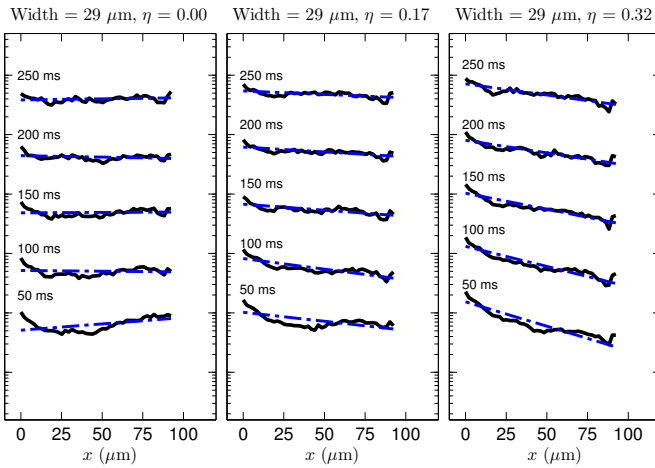


FIG. 2. $29 \mu\text{m}$ width channel density profile data. Channel profiles from 50 ms to 250 ms are plotted on a semilogarithmic scale, together with a linear fit to the logarithmic data. This data is an average of three experimental disorder realisations.

IV. SIMULATIONS FOR LONG TIMES

We show in Fig. 8 simulations conducted for long times for the same conditions as Fig. 2 of the main manuscript. The data show that in the case of $\eta = 0.07$, a long-time exponential density profile is not obtained, but the density profile remains exponential for $\eta = 0.17$ and $\eta = 0.32$. We note that this exponential character remains, despite complications from higher energy atoms re-entering the channel from the drain reservoir.

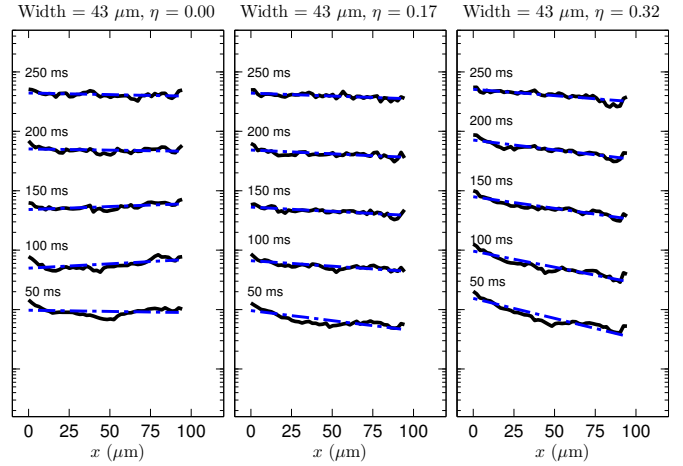


FIG. 3. $43 \mu\text{m}$ width channel density profile data. Channel profiles from 50 ms to 250 ms are plotted on a semilogarithmic scale, together with a linear fit to the logarithmic data. This data is an average of three experimental disorder realisations.

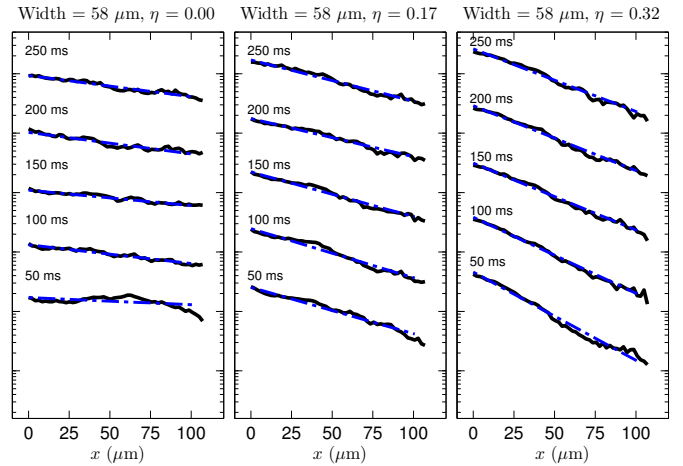


FIG. 4. $58 \mu\text{m}$ width channel density profile data. Channel profiles from 50 ms to 250 ms are plotted on a semilogarithmic scale, together with a linear fit to the logarithmic data. This data is an average of three experimental disorder realisations.

V. MOMENTUM DISTRIBUTIONS

We extend the momentum distributions plotted in Fig. 3 of the main manuscript in Fig. 9, by including the momentum distributions along the x -axis within the channel, derived from numerical simulation. (The x -axis is the direction along the channel, and a positive value means that k_x is directed towards the drain). This data also gives information regarding the direction of wave propagation, and allows us to draw conclusions regarding the scattering. The data collection time of 125 ms is chosen so as to be prior to atoms from the drain reflecting

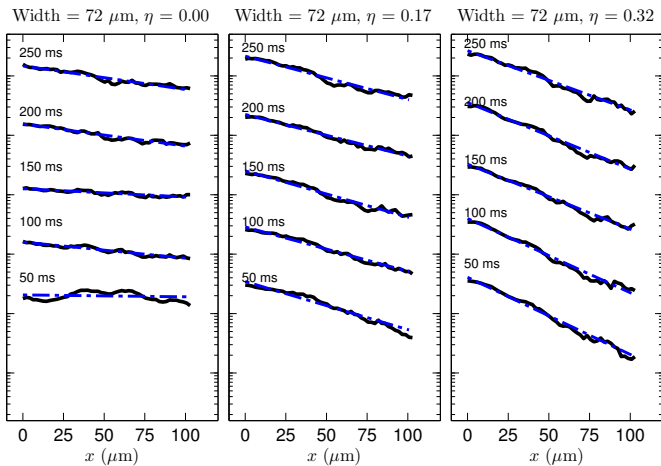


FIG. 5. **72 μm width channel density profile data.** Channel profiles from 50 ms to 250 ms are plotted on a semilogarithmic scale, together with a linear fit to the logarithmic data. This data is an average of three experimental disorder realisations.

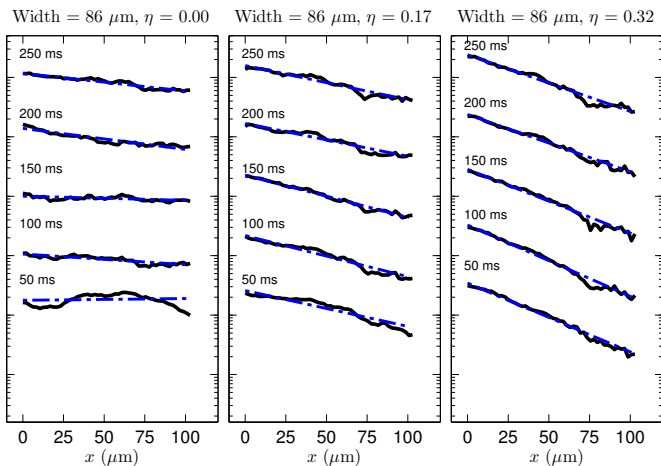


FIG. 6. **86 μm width channel density profile data.** Channel profiles from 50 ms to 250 ms are plotted on a semilogarithmic scale, together with a linear fit to the logarithmic data. This data is an average of three experimental disorder realisations.

and re-entering the channel.

In the case of zero disorder, only atoms with a positive k_x value are present within the channel, as can be readily understood from the system geometry. In the case of disorder, scattering alters the direction of k , which smooths the k_x distribution. Moreover, we observe a bimodal distribution, consisting of a narrow distribution centred at $k_x = 0$, on top of a far broader distribution. This is further evidence that the channel contains atoms with a range of energies, with atoms in the narrow low-energy distribution experiencing exponential localisation and those in the higher energy distribution subject to weak localisation.

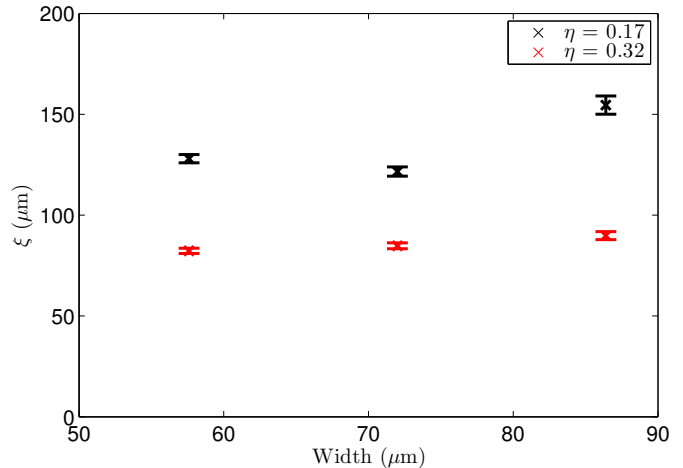


FIG. 7. **Dependence of localisation length on width for a quasi-2D environment.** The experimental localisation length as an average from 210-250 ms of expansion time is plotted for the width data shown in Figs. 4-6, for $\eta = 0.17$ and $\eta = 0.32$, with $L = 108 \mu\text{m}$. The error bars show the standard error in the mean over the three disorder configurations.

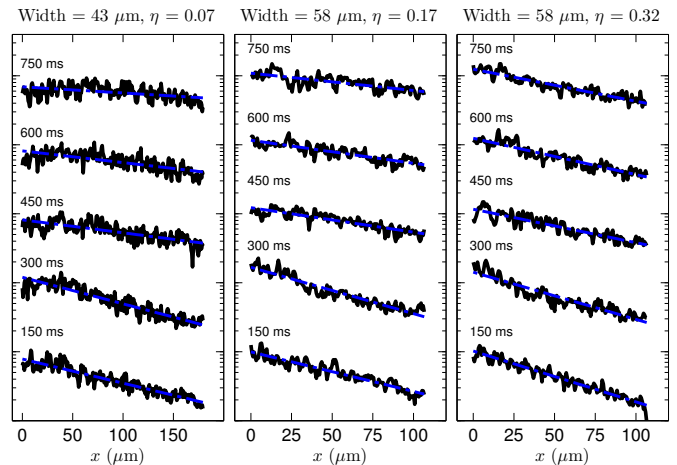


FIG. 8. **Long-time simulations.** Simulations for the conditions in Fig. 2 of the main manuscript, plotted semilogarithmically for long times. The simulations are overlaid with exponential fits to the data. Offsets by increasing factors of 10 are for clarity.

VI. POTENTIAL SLICES

Figure 10 shows single slices of the potential applied to the spatial light modulator, as used in the experiment for three fill-factors. Each point scatterer occupies 2 pixels along the x -direction. Equivalent potentials are used for the numerical simulation. On average, a single slice will yield a fraction η of pixels within the channel of greyscale 255.

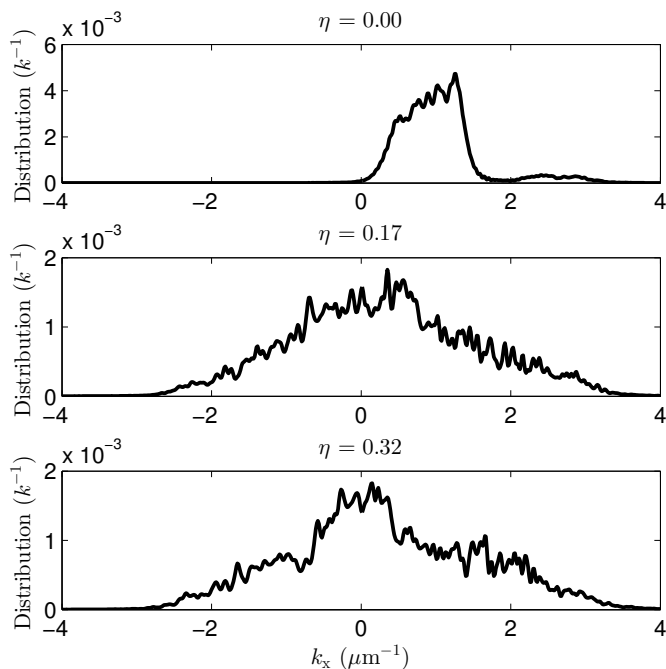


FIG. 9. **Channel momentum distributions.** The momentum distributions along x within the channel are obtained after 125 ms of expansion for three different fill-factors, with $(r, L, w) = (43, 108, 58)$ μm , via numerical simulation.

VII. RESERVOIR CAPACITANCE

The channel resistance is found from the initial flow of atoms into the drain reservoir, according to

$$\frac{d\Delta N}{dt} = -\frac{\Delta N}{RC}$$

with the reservoir capacitance given by [3]

$$C = \frac{3 \left(\frac{1}{2}N\right)^{1/3}}{4\alpha},$$

the constant α is

$$\alpha = \left[\frac{g \left(\frac{1}{2}m\omega_z^2\right)^{1/2}}{\frac{4}{3}\pi r^2} \right]^{2/3},$$

and $g = 4\pi\hbar^2 a_s/m$ is the 3D nonlinearity, r is the reservoir radius, m is the mass of an atom, N is the number of atoms, and ω_z is the vertical trapping frequency. In our system with $r = 43$ μm , $\hbar C = 19$ s.

VIII. COMPARISON BETWEEN ORDERED AND DISORDERED SCATTERERS

For comparison, we use the tuneability of the spatial light modulator to compare a disordered system with an ordered system, in a regime of weak localisation. In

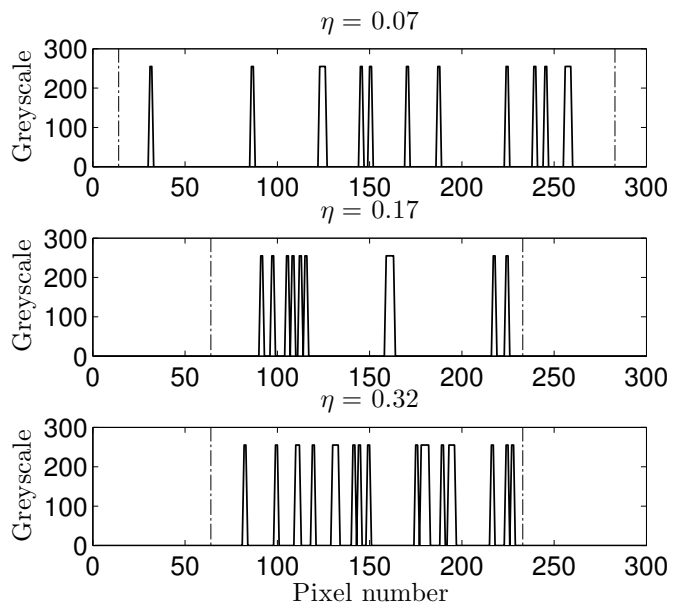


FIG. 10. **Slices of dumbbell potential.** Single slices of the potentials plotted in Fig. 2(a)-(c) of the main text are shown here, along the x -direction. Dash-dot lines indicate the mouth of the channel.

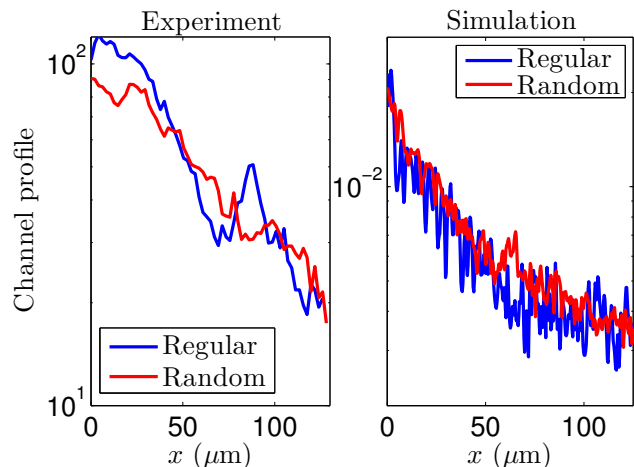


FIG. 11. **Long-time density profile in regular and random lattices** (a) Experimental data. The density at fill-factor $\eta = 0.13$, $(r, L, w) = (43, 162, 43)$ μm is shown for scatterers arranged randomly, compared with scatterers arranged in a square regular lattice. (b) Numerical simulation, with equivalent parameters for (a).

Fig. 11(a), we compare the experimental density profiles obtained when the same number of point scatterers ($\eta = 0.13$) are arranged randomly, compared to in a regular ordered square lattice. We observe stronger linearity in the semilogarithmic plot for the disordered case. The R^2 value of the semilogarithmic profile in the regular channel is 0.90, compared with 0.95 of the disordered channel. We also point out the curvature observed in the first 20 μm in the case of regular scatterers.

Name	Symbol	Value
particle number	N	16000
^{87}Rb mass	m	$87 \times \text{amu}$
Trap frequency (x)	ω_x	$2\pi \times 1 \text{ rad/s}$
Trap frequency (y)	ω_y	$2\pi \times 1 \text{ rad/s}$
Trap frequency (z)	ω_z	$2\pi \times 800 \text{ rad/s}$
angular frequency of initial trap	ω_0	$2\pi \times 25 \text{ rad/s}$
s -wave scattering length	a_s	$107a_0$
nonlinearity length	λ	$2\sqrt{2\pi} Na_s$
angle of effective gravity	θ	0.0002°
potential depth	V_{db}	22 nK
scatterer strength	V_{sc}	5 nK

TABLE I. Physical parameters in the numerical simulation.

The increased exponential character of the density profile in the disordered lattice is also found in the simulation (Fig. 11(b)), and the simulation indicates that the resistance of the disordered lattice ($1.7 \times 10^{-3}h$) is 20% larger than the regular lattice ($1.4 \times 10^{-3}h$). We note the high-frequency spatial oscillation present in the simulated regular-lattice density profile, which we do not observe in the experiment due to the imaging resolution. A full study of the comparison between regularly arranged and random scatterers is currently in preparation.

IX. NUMERICAL SIMULATION

We provide the values of physical parameters used in the simulation in Table I, and the numerical parameters in Table II. We solve the Gross-Pitaevskii equation

$$i\hbar \frac{\partial \psi(\mathbf{r}, t)}{\partial t} = \left[-\frac{\hbar^2}{2m} \nabla_{2\text{D}}^2 + V_{\text{trap}}(\mathbf{r}, t) + V_{\text{int}}(\mathbf{r}, t) \right] \psi(\mathbf{r}, t)$$

with initial condition $\psi(\mathbf{r}, t) = \psi_0(\mathbf{r})$. Here $V_{\text{int}}(\mathbf{r})$ denotes the interaction potential

$$V_{\text{int}}(\mathbf{r}) = gN |\psi(\mathbf{r})|^2 = \frac{2\sqrt{2\pi} \hbar^2 a_s}{ma_z} N |\psi(\mathbf{r})|^2,$$

with a_s being the s -wave scattering length of the ^{87}Rb atoms, a_z is the oscillator length of the harmonic oscillator corresponding to ω_z . The trapping potential, $V_{\text{trap}}(\mathbf{r})$, includes the strong dumbbell-shaped well of average depth V_{db} , the artificial gravitational potential and a weak harmonic potential with minimum at the centre of the dumbbell. We also note here that the presence of the linear tilt causing the artificial gravitational potential, and of the weak harmonic trap in the numerical simulation are included in the calculations for consistency with the experimental setup. The interference fringes due to distortion of the 1064 nm beam wavefront within the 2D trap are not modelled.

The initial wavefunction is the ground-state wavefunction of N interacting particles in a three-dimensional

harmonic potential with angular frequencies ω_0 . This ground-state wavefunction, $\psi_0(\mathbf{r})$, is determined by the standard imaginary-time propagation method [4, 5], and is shifted to the source reservoir. In most of the simulation its centre is located at the opening of the channel. However, we note that the exact position does not strongly influence the transport properties, and only moderately affect the timing. Using the adaptive, fourth-order Runge-Kutta-Fehlberg method[6] we propagate this initial wavefunction (reduced to a 2D wavefunction) in real time over a grid of size $n_x \times n_y$ representing the rectangular area $L_x \times L_y$ in real space. Here we mention that unlike the popular fourth order Runge-Kutta method (RK4), the Runge-Kutta-Fehlberg method (RKF45) is an adaptive method, i.e., it chooses the best step-size to meet a predefined error threshold. Therefore the time-step varies during in our simulations to meet the error threshold of 7×10^{-12} in L_2 -norm of the wavefunction. The dumbbell—for any channel length and circular reservoir radius—is positioned at the centre of this grid symmetrically, i.e, the centre of the channel is at the centre of the numerical grid.

X. EFFECT OF INTERACTIONS

In Fig. 12 we conduct numerical simulations for a range of interaction strengths, to determine the effect of interactions on Anderson localisation. The simulations are performed by allowing the atoms to expand from the condensate with scattering length a_{Rb} . Once the atoms have filled the first reservoir, they have acquired their initial k -vector distribution, and at this point in the simulation the interaction strength is abruptly changed to a multiple of a_{Rb} .

We observe no significant difference in the localisation lengths obtained with scattering lengths 0 and a_{Rb} , indicating that we may view the system as near-non-interacting. This is due to the very low atomic density, averaging approximately 1 atom / μm^2 .

We observe that for $a \leq 4a_{\text{Rb}}$, the measured apparent localisation length tends to a steady state in time. For $a > 6a_{\text{Rb}}$, we observe that the channel density profile does not tend to a steady localised state, and instead exhibits a characteristic $\xi \sim \sqrt{t}$, indicative of diffusive

Name	Symbol	Value
Spatial extension of the numerical grid in the x direction	L_x	500 μm
Spatial extension of the numerical grid in the y direction	L_y	225 μm
Number of grid points in the x direction	n_x	1536
Number of grid points in the y direction	n_y	768

TABLE II. Parameters for the numerical simulation.

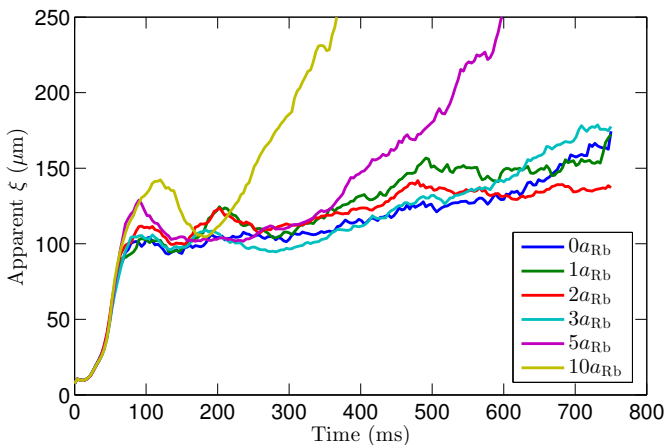


FIG. 12. **Effect of interaction strength on localisation length.** Apparent localisation lengths as a function of time are plotted for a range of interaction strengths, with scattering lengths ranging from 0.0 – $10 a_{\text{Rb}}$, as determined by numerical simulation. For this data, $(r, L, w) = (43, 108, 58) \mu\text{m}$ and $\eta = 0.32$.

expansion. These results indicate that the experiment is conducted in a weakly-interacting regime in which interactions do not significantly affect Anderson localisation.

We note that the slow apparent increase in localisation length for $t > 400$ ms is due in large part to atoms which re-enter the channel from the drain reservoir, and it does not imply a weakening of Anderson localisation.

XI. RELATIONSHIP BETWEEN ℓ_s AND ℓ_{tr}

The elastic mean free-path between scattering events is approximately given by the mean spacing between scatterers $\ell_s = \sigma/\sqrt{\eta}$, while the transport mean free path, ℓ_{tr} , also known as the Boltzmann mean free path, is the distance over which the memory of the initial direction is lost. It is found [7] that $\ell_{\text{tr}} = \Lambda(k\sigma)\ell_s$, with a proportionality constant Λ dependent on relative size of a scatterer σ and the de Broglie wavelength $\lambda = 2\pi/k$. Based on the data in Fig. 3(e) of the main text, $k\sigma \approx 1$ for the peak value of k within the channel. We emphasise that there is a distribution of atomic energies in our sample and that Λ depends strongly on $k\sigma$.

First let us determine a few characteristic quantities derived from classical or semi-classical approximations. One length scale is provided by the average momentum of atoms within the channel, as found from Fig. 3(e) of the main text:

$$\lambda_{\text{dB}} = \frac{2\pi}{k} \approx 3.9 \mu\text{m}. \quad (1)$$

Within the channel, the de Broglie wavelength is significantly larger than the scatterer size $\sigma \approx 1.44 \mu\text{m}$. The physical system also possesses other characteristic length scales: the length of the disordered channel

$L_0 \approx 36 - 180 \mu\text{m}$, the channel width $w \approx 14 - 87 \mu\text{m}$, and the mean minimal distance between scatterers $\ell_s = \sigma/\sqrt{\eta} \approx 2.5 - 3.4 \mu\text{m}$ for the corresponding fill-factors $\eta = 0.32$ and 0.17 , respectively. In general, therefore, their relationship in the sequence of our experimental runs is $\sigma \lesssim \ell_s < \lambda_{\text{dB}} \lesssim \ell_{\text{tr}} < w < \xi \lesssim L_0$.

As for length scales, there are also some characteristic energy scales of this system which are given below as temperatures. Furthermore for all length scales we may associate an energy scale as well via energy $\propto \hbar^2/m(\text{length})^2$. We estimated the condensate temperature to be $T_{\text{BEC}} \approx 5$ nK, and the BEC is released in a dumbbell-shaped potential with depth of $T_{\text{pot}} \approx 22$ nK. The random scatterers have a height of $T_{\text{sc}} \approx T_{\text{pot}} \approx 5$ nK. Out of these energy scales we note here the highest which corresponds to σ , the shortest length scale: $E_\sigma = \hbar^2/m\sigma^2 \approx 2.7$ nK.

The scattering process has a decisive parameter, $k\sigma$, i.e., the relative size of the matter-wave compared to a single scatterer. Using the approximation, $k \approx k_{\text{dB}}$, one obtains $k_{\text{dB}}\sigma \approx 2.2$. Such value of $k\sigma$ suggests a non-isotropic scattering process even though we are still in the weak scattering regime since the atoms kinetic energies are higher than $E_{\text{sc}} = \eta E_\sigma$ for all η values.

In order to establish a relationship between ℓ_{tr} and ℓ_s we evaluate Eq. (6) in Ref. [7]

$$\frac{1}{\Lambda(k\sigma)} = \frac{\ell_s}{\ell_{\text{tr}}} = 1 - \frac{\int_0^{2\pi} \cos(\theta) \mathcal{P}(k\sigma, \theta) d\theta}{\int_0^{2\pi} \mathcal{P}(k\sigma, \theta) d\theta} \quad (2)$$

where $\mathcal{P}(k\sigma, \theta) = 8\mathcal{F}(k\sigma \sin(\theta/2))$ and $\mathcal{F}(x) = [\arccos(x) - x\sqrt{1-x^2}] \Theta(1-x)$, while Θ denotes the Heaviside distribution.

Figure 13 shows the ratio of the transport mean free path ℓ_{tr} to the scattering mean free path ℓ_s , as a function of the wavenumber $|k|$. As $k\sigma \rightarrow 0^+$ the function \mathcal{P} is more or less constant 4π . In this limit one may utilise that $\mathcal{F}(x) \sim \frac{\pi}{2} - 2x + \frac{1}{3}x^3$ and determines the integrals in Eq. (2) analytically to obtain

$$\frac{\ell_{\text{tr}}}{\ell_s} \sim 1 + \frac{8}{3\pi^2}(k\sigma) + \frac{256}{9\pi^4}(k\sigma)^2 \quad \text{as } (k\sigma) \rightarrow 0^+.$$

In the opposite limit, $k\sigma \rightarrow \infty$, the Heaviside distribution in \mathcal{F} is non-zero for $0 \leq \theta \leq 2\arcsin(1/k\sigma) \approx 2/k\sigma$ or $2\pi - 2/k\sigma \leq \theta \leq 2\pi$. Therefore the bounds of integrals in Eq. (2) are also restricted to these two small intervals. However, the few leading terms in the Taylor expansion of \mathcal{F} are not sufficient to determine the asymptotic behaviour of $\Lambda(k\sigma)$, but one needs to retain all terms in the expansion

$$\mathcal{F}(x) = \frac{\pi}{2} - 2x + \sum_{n=1}^{\infty} \frac{1}{2^{2n-1}(2n-1)(2n+1)} \binom{2n}{n} x^{2n+1}.$$

The leading term of $\Lambda(k\sigma)$ is quadratic, $c_2(k\sigma)^2$, where the explicit expression of c_2 cannot be given in finite terms. Its value is approximately

$$c_2 \cong \frac{4}{3} \frac{6\pi - 11}{6\pi - 16} \approx 3.673$$

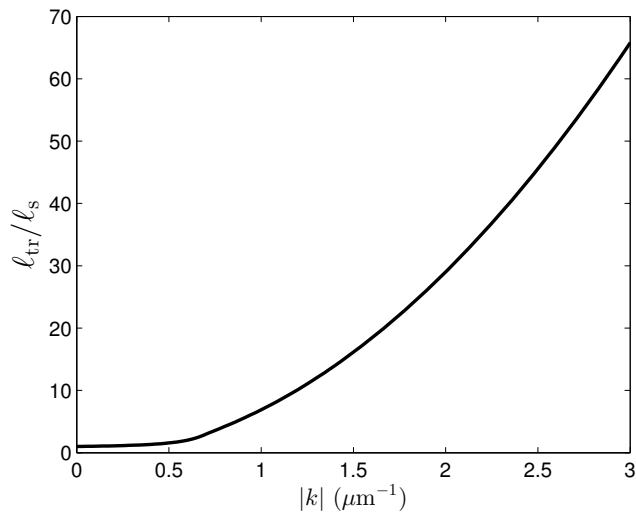


FIG. 13. **Λ as a function of wavenumber.** The ratio of the transport mean free path ℓ_{tr} to the scattering mean free path ℓ_s is plotted as a function of $|k|$, where σ is assumed to be $1.4 \mu\text{m}$. For $|k| = 1.0 \mu\text{m}^{-1}$, $\ell_{tr} \approx 7\ell_s$.

At the end we may evaluate the analytic first order correction [7] to the Boltzmann diffusion coefficient for an indicative value of the fill-factor, $\eta = 0.06$,

$$\frac{\delta D}{D_B} = \frac{2}{\pi} \frac{\ln(L_0/\ell_s)}{k\ell_{tr}} \approx 3.6 \times 10^{-3}.$$

-
- [1] D. S. Petrov, M. Holzmann, and G. V. Shlyapnikov, Phys. Rev. Lett. **84**, 2551 (2000).
- [2] P. Krüger, Z. Hadzibabic, and J. Dalibard, Phys. Rev. Lett. **99**, 040402 (2007).
- [3] A. Li, S. Eckel, B. Eller, K. E. Warren, C. W. Clark, and M. Edwards, Phys. Rev. A **94**, 023626 (2016).
- [4] W. Bao and Q. Du, SIAM J. Sci. Comput. **25**, 1674 (2004).
- [5] W. Magnus, Commun. Pure Appl. Math **7**, 649 (1954).
- [6] R. Burden and J. Faires, *Numerical Analysis* (Brooks/Cole, Cengage Learning, 2011).
- [7] R. C. Kuhn, C. Miniatura, D. Delande, O. Sigwarth, and C. A. Müller, Phys. Rev. Lett. **95**, 250403 (2005).